

Monolithic Perovskite/Silicon Tandem Solar Cells

Steve Albrecht¹, Michael Saliba², Juan-Pablo Correa-Baena², Klaus Jäger¹, Lars Korte¹, Anders Hagfeldt², Michael Grätzel², and Bernd Rech¹, ¹Helmholtz-Zentrum Berlin für Materialien und Energie GmbH, ²Swiss Federal Inst. of Technology (EPFL) Lausanne

ABSTRACT

Silicon photovoltaics is one of the most important solar energy conversion technology. Improving silicon solar cells, however, is becoming increasingly challenging as this technology approaches its practical efficiency limit. Organic–inorganic perovskite materials, such as $\text{CH}_3\text{NH}_3\text{PbI}_3$, have become attractive for tandem cell integration with crystalline silicon (c-Si), because the combination of perovskite and silicon optical band gaps is well suited for harvesting the solar spectrum. The perovskite/c-Si tandem technology can offer an inexpensive option to boost state-of-the-art silicon single junctions well above the practical limit. Additionally, due to the high voltage at the maximum power point, this tandem design is suitable for low-cost water splitting and CO_2 reduction. So far, the highest reported perovskite solar cells require high temperature processing ($>500^\circ\text{C}$) incompatible with the currently best performing silicon technology: the silicon heterojunction (SHJ). Here, we highlight the effort that has been undertaken with regard to this monolithic tandem technology and we present a monolithic, 2-terminal perovskite/SHJ tandem solar cell with a planar perovskite top-cell using a low temperature electron selective contact in combination with a SHJ bottom cell. Our tandem cell enables close to 20% efficiency in the reverse scan and 18% stabilized power output. We furthermore perform optical simulations on experimentally relevant tandem stacks that give guidelines to achieve efficiencies above 28%, even with flat interfaces in the absence of light trapping schemes.

INTRODUCTION

Solar cells made from organic-inorganic perovskites, such as methylammonium-lead-triiodide ($\text{CH}_3\text{NH}_3\text{PbI}_3$), have shown tremendous power conversion efficiency (PCE) enhancements from 3.8 to over 22% during the last six years.¹⁻³ No other solar cell technology has shown such spectacular improvements in a comparable time frame.^{4,5}

Organic-inorganic perovskite materials are promising solar cell absorbers as they show unique optoelectronic properties and can be processed from solution enabling low cost, high throughput fabrication at low temperatures on flexible substrates.^{6,7} Organic-inorganic perovskites typically show the ABX_3 structure that is illustrated in Figure 1. Here, A is the organic cation that is most often methylammonium or formamidinium, or a mixture of both. Recently the organic cation was frequently partially exchanged by the inorganic cation caesium.^{8,9} B is the central metal, e.g. lead or tin, that is surrounded by X, the octahedral halide, e.g. iodine, bromine, chlorine, or a mixture of the halides.

The optical band-gap of the commonly used $\text{CH}_3\text{NH}_3\text{PbI}_3$ is 1.57 eV and can be tuned via halide replacement¹⁰ or cation exchange.¹¹ The perovskite material has a high absorption coefficient across the entire visible range together with a sharp onset and very low absorption of sub band-gap features.¹² Hence, a perovskite layer thickness of around 500 nm is sufficient to absorb a very high portion of the incident visible light⁵ and transmits a high fraction of NIR light. The exciton binding energy at room temperature is negligible,¹³ and the carrier diffusion length exceeds the active layer thickness.^{14,15} Also, charge transport across the entire active

layer is not limiting the device performance with a charge carrier mobility in the order of $10 \text{ cm}^2/\text{Vs}$.^{16,17} Due to the strongly reduced recombination in the bulk^{16,18} and at the surface,¹⁹ the free charge carriers that are formed directly upon photoexcitation are efficiently extracted from the device. This enables internal quantum efficiencies close to 100%,²⁰ a high fill factor (FF) above 80%, and open circuit voltage (V_{oc}) only 400 mV below the potential of the optical band-gap,²¹ resulting in a record efficiency above 22%.³

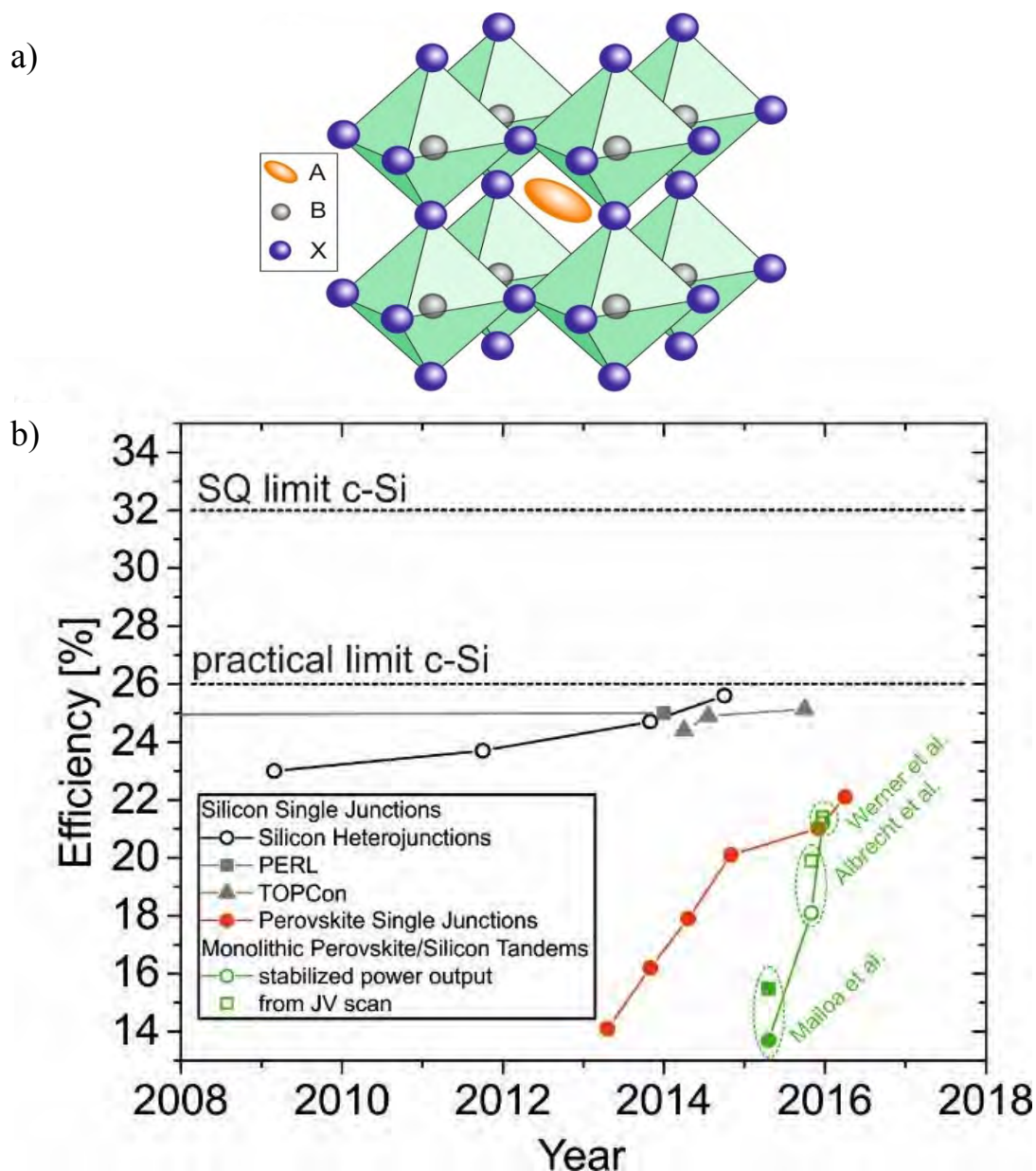


FIG. 1: (a) Schematic ABX_3 crystal structure of organic-inorganic perovskites with A being the organic cation (methylammonium, formamidinium), B the metal (lead, tin) and X the halide (iodine, bromine, chlorine). (b) Certified or published record efficiencies over time for various PV technologies including silicon and perovskite single junctions according to Refs. 3,5,22-24 together with the published monolithic perovskite/silicon tandem cells according to Refs. 25-27. Filled symbols refer to device designs using $>200^\circ\text{C}$ temperature during device processing. Open symbols refer to low temperature ($<200^\circ\text{C}$) processing routes.

These unique optoelectronic properties make organic-inorganic perovskites perfect candidates for tandem cell integration in combination with crystalline silicon (c-Si). In the c-Si/perovskite tandem cell, higher energy photons are absorbed by the perovskite sub-cell and converted at a high voltage without significant losses from thermalization. Infrared photons are transmitted through the perovskite and photo-generate free charges in the c-Si sub-cell. Thus, a wide spectral range up to 1.12 eV, defined by the band-gap of c-Si, can be covered by the tandem cell. This tandem design has a detailed-balance limit of ca. 40%,²⁸ hence overcoming the Shockley-Queisser limit for silicon single junctions of around 32%.²⁹

The monolithic (2-terminal) integration of perovskite and c-Si has several advantages. First, the number of contacts that enable lateral current flow is lower than in a 4-terminal device. Therefore, less conductive layers can be applied in the interconnection contact that have less parasitic absorption effects. Secondly, only one substrate, i.e. the silicon wafer itself is used during production, which may reduce processing costs. Thirdly, the tandem device operates at a higher voltage with a lower current, when both sub-cells are connected in series, which further enables fewer losses from series resistance. Finally, only one electrical circuit is needed which makes the use of only one junction box and inverter necessary. However, this design may have the disadvantage of being affected by spectral changes or different angles of incident of the sunlight during operation. When the device is optimized such that current matching is realized under AM 1.5G at normal incidence, the photocurrent under real non-optimized conditions might be limited by one of the sub-cells producing less current. Furthermore, processing in a monolithic stack is more complex as in 4-terminal tandem cell with independently processed substrates. The range of processing parameters, e.g. temperature and solubility, in the monolithic architecture is restricted by the stability of the layers underneath.

SUMMARY OF RESULTS

The first monolithic perovskite/c-Si tandem was realized by Mailoa, Bailie and co-workers and published in March 2015.²⁵ They used a diffused silicon homojunction cell with an intermediate tunnel recombination contact formed by highly n-doped amorphous hydrogenated silicon, (n⁺⁺)a-Si:H that was deposited on the diffused p⁺⁺ emitter and then partially crystallized in a high temperature step. Silver nanowires were implemented as top contact, similar to the 4-terminal device, in a previous publication by Bailie et al.³⁰ This resulted in a stabilized efficiency of 13.7% with a V_{oc} of 1.56 V. This efficiency is lower than that of their reported 4-terminal device, which is partially caused by the parasitic light absorption of the doped spiro-OMeTAD layer.²⁵ The parasitic absorption complicates the realization of current matching, being a prerequisite to achieve high efficiencies in monolithic tandem cells.

Most of the high efficiency perovskite single junctions use compact and/or mesoporous TiO₂ that is typically sintered at high temperatures of 500°C. Devices employing this mesoporous TiO₂ scaffold yielded the highest power conversion efficiencies (PCEs) up to date,^{5,9} with least pronounced hysteretic behaviour as compared to planar devices without the use of mesoporous TiO₂.² Unfortunately such a high temperature is not suitable for a-Si:H/c-Si silicon heterojunction (SHJ) cells. Owing to the high surface passivation quality induced by (i)a-Si:H, SHJ solar cells can have high open circuit voltages up to 750 mV,²² which is significantly higher as compared to diffused homojunction cells showing a maximum V_{oc} around 700 mV. However, a major limitation is the thermal stability of a-Si:H: The hydrogen, which passivates the amorphous network, becomes mobile at around 200°C and eventually effuses, reducing the passivating quality of the a-Si:H/c-Si interface and thus the device performance. Therefore, in the monolithic integration of perovskite and SHJ solar cells, high temperature sintering of the mesoporous or compact TiO₂ layer is not feasible. One option to

solve this problem would be a planar, i.e. mesoporous-free perovskite sub-cell with an electron-selective contact processed at low temperatures. However, there are only a few reports showing planar, low-temperature devices with a stabilized high efficiency output in the regular device architecture in which the electron selective contact is processed on top of the transparent conductive oxide (TCO).³¹⁻³³ Recently, a new approach for manufacturing planar perovskite solar cells at temperatures below 120°C using atomic layer deposited (ALD) SnO₂ as electron selective contact was developed by Correa-Baena and coworkers.³⁴ Almost hysteresis-free solar cells with PCEs over 18% efficiency, being fully compatible with silicon heterojunctions, were realized.³⁴

We combined the planar perovskite single junction with SnO₂ electron selective contacts formed by ALD, as developed by Correa-Baena and co-workers, with a silicon heterojunction into a monolithic tandem cell. In October 2015, we published the monolithic perovskite/silicon heterojunction tandem solar cell that was processed at low temperatures.²⁷ Figure 2(a) schematically displays the device design: a double-side polished n-type silicon wafer was used to fabricate the silicon bottom cell. Thin layers of intrinsic and doped a-Si:H were deposited via plasma enhanced chemical vapour deposition (PECVD), in order to form a p-n junction and back surface field (BSF) on the front and rear of the wafer, respectively. Next, an indium tin oxide (ITO) layer, which connects both sub cells, was deposited on the front side by means of sputtering through shadow masks. The back side was fully covered with aluminium-doped zinc oxide (AZO) and silver, both deposited by sputtering. On the front side, SnO₂ was deposited via ALD. The perovskite was processed by a one-step spinning process and the doped spiro-OMeTAD layer by spin coating. Then a MoO₃ layer was deposited via thermal evaporation as a buffer layer and finally the top ITO contact is sputtered through the same shadow mask as used for the first ITO layer connecting both sub-cells. Both ITO layers are aligned exactly on top of each other. The active area is defined by the aligned ITO areas, as indicated by the red dashed lines in Figure 2(a). To reduce the reflection at the air/front ITO interface, LiF was thermally evaporated onto the finished cell.

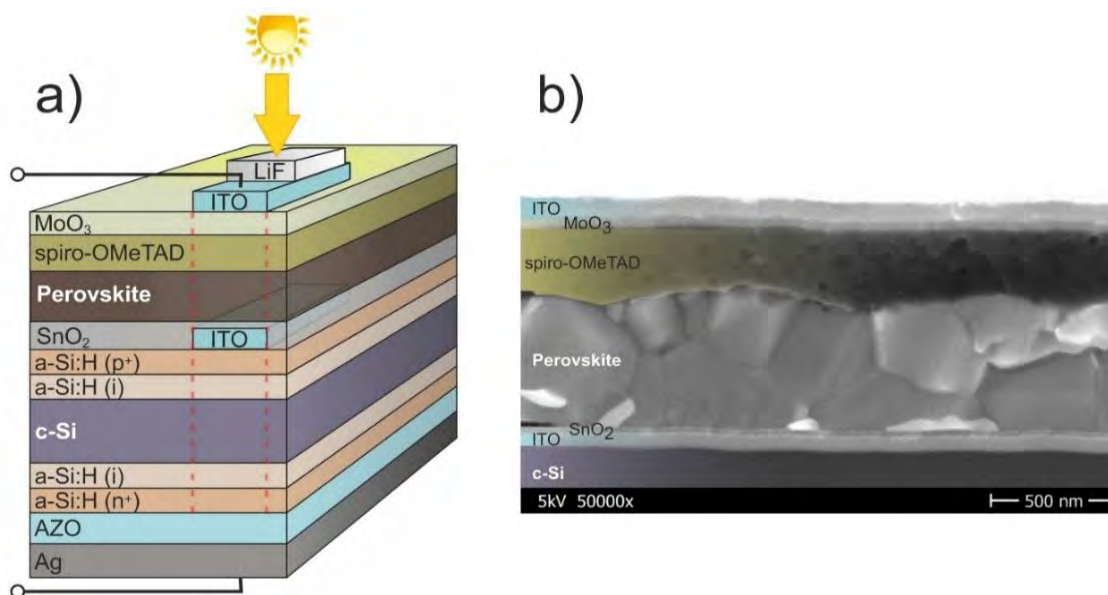


FIG. 2: (a) Schematic device design of the silicon heterojunction/perovskite tandem solar cell. The red dashed line indicates the active area. (b) Cross sectional scanning electron micrograph of a typical monolithic tandem solar cell. (Reproduced from Ref. 27 with kind permission from The Royal Society of Chemistry.)

Figure 2(b) displays a previously published scanning electron micrograph (SEM) cross section image of the upper part of the tandem cell structure.²⁷ The individual layers can be clearly identified. In the very bottom of the image, the silicon wafer is found. On top, the interconnecting contact formed by ITO and SnO₂ is seen. The perovskite crystals show vertical sizes of several hundreds of nanometres. Some crystals extend throughout the complete film, for example on the left side of the image. The spiro-OMeTAD layer covers the perovskite film uniformly and the transparent top contact formed by MoO₃ and ITO completes the device.

In the monolithic tandem device, light travels through the top contact and the spiro-OMeTAD layer before being absorbed in the perovskite layer. This is different from typical perovskite single-junction geometries.³⁵ Doped spiro-OMeTAD has broad absorption peaks at 380 nm and 500 nm,³⁶⁻³⁸ which cause observable parasitic absorption²⁵ and reduce the photocurrent, especially below 400 nm. Figure 3(b) displays the external quantum efficiency (EQE) spectra for the monolithic tandem cell, recorded with bias light to selectively address the sub-cells. The overall EQE is 60-78%; especially in long wavelength range interference fringes are detected. Also indicated is the integrated current calculated from the EQE spectra assuming AM 1.5G illumination for each sub-cell. Comparing the currents generated from the sub-cells, it follows that the silicon sub-cell is the current limiting one. Both sub-cells together generate a short-circuit current density (J_{sc}) of 28.7 mA/cm², which is lower than the J_{sc} of the reference silicon single junction cell (31 mA/cm²). Thus optical losses limit the tandem cell due to the flat interfaces and non-optimized layer thicknesses in the present cell design. The reflectivity shown in Figure 3(b) is rather high with ca. 10% reflection throughout the perovskite absorption range and up to 25% in the NIR regime, especially when no anti-

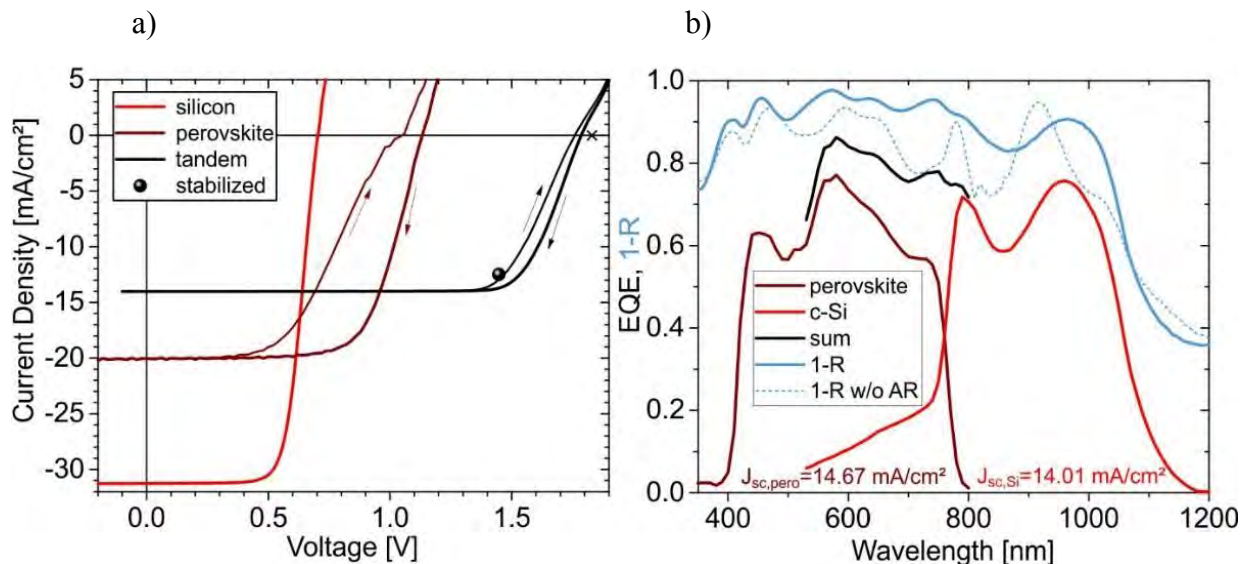


FIG. 3: (a) *JV* characteristics: The red line shows the characteristics of the silicon single junction cell and the brown line corresponds to the perovskite reference single junction cell with non-transparent Au contacts in forward and reverse scan (as indicated by the arrows). The black curve shows values for the monolithic tandem cell with additional LiF anti-reflectance (AR) coating. The black cross indicates the sum of the V_{oc} of the reference single-junctions (b) External quantum efficiency (EQE) of the individual sub-cell in the monolithic tandem device with AR coating. Also shown are the sum of the individual EQE spectra, the currents from integration of the EQE, and 1-R of the complete monolithic stack with and without AR coating. (Reproduced from Ref. 27 with kind permission from The Royal Society of Chemistry.)

reflectance (AR) layer is used. The transparent and low refractive index material lithium fluoride (LiF) strongly reduces the reflection losses at the air/ITO interface and enhances the photocurrent in the silicon sub-cell by about 1.5 mA/cm². With the AR coating, the sub-cells are almost current matched with current densities of 14.7 and 14.0 mA/cm² for the perovskite and silicon sub-cell, respectively, under AM 1.5G illumination.

Device	J_{sc} (EQE) ^a [mA/cm ²]	J_{sc} [mA/cm ²]	V_{oc} [mV]	FF [%]	PCE [%]
Tandem Cell:	14.67 / 14.01				
reverse scan ^b		11.8	1785	79.5	16.8
forward scan ^b		11.8	1759	77.3	16.1
reverse scan ^c		14.0	1785	79.5	19.9
forward scan ^c		14.0	1759	77.3	19.1
stabilized efficiency ^d					18.1
Single Junctions:^e					
Silicon (1 cm ²) ^f		31.3	703	71.4	15.7
perovskite reverse ^g		20.1	1130	68.3	15.5
perovskite forward ^g		20.1	1048	49.3	10.4

Table 1: Performance data of the best performing tandem device with AR coating and of the single junctions for comparison. Due to hysteresis of the perovskite solar cells, different bias scanning directions were used at a scan rate of 500mV/s from V_{oc} to J_{sc} (reverse) and from J_{sc} to V_{oc} (forward), respectively. (Reproduced from Ref. 27 with kind permission from The Royal Society of Chemistry.)

^a from integration of the EQE of the respective sub-cell measured with background bias light, 1st value: perovskite, 2nd value: silicon; ^b measured with an aperture mask under simulated AM 1.5G illumination calibrated to 100 mW/cm²; ^c the measured J_{sc} is adjusted to match the value of the limiting sub-cell as determined from the EQE spectra (see text); ^d the stabilized efficiency is deduced from the current transient measurements at $V_{MPP} = 1.45$ V; ^e single reference junctions in standard device configuration; ^f 1 cm² active area with metal grid; ^g 0.25 cm² active area with non-transparent Au contacts.

Figure 3(a) shows our recently published JV characteristics,²⁷ measured for the monolithic tandem cell and the reference single-junctions, i.e. the silicon heterojunction and the perovskite cell in standard configuration with opaque gold electrode. The corresponding performance data can be found in Table 1. The device design of the silicon heterojunction reference cell is comparable to that used in the tandem configuration except that a metal grid on top of the ITO is applied to effectively collect the current from the complete active area (1 cm²). The planar wafer that is used here leads to several mA/cm² lower J_{sc} as compared to standard SHJ cells,³⁹ since the light trapping induced by a random pyramid texture on the wafer in such cells is absent here. Also, the V_{oc} and FF are reduced with respect to our textured reference cells. This is most likely due to different PECVD growth conditions of the a-Si:H on flat wafers, leading to a decreased a-Si:H/c-Si interface passivation and reduced conductivity/increased contact resistance.

The perovskite single junction fabricated on glass/ITO substrates achieved a high V_{oc} of 1.13 V, comparable to the high values reported when utilizing a SnO₂ electron selective contact that is energetically well aligned with the conduction band of the perovskite.³⁴ Together with a FF of 68.3% and a J_{sc} of 20.1 mA/cm² this results in an efficiency of 15.5%. The high V_{oc} of the perovskite single junction is beneficial for the tandem device. However, a more pronounced hysteresis is measured for the perovskite cell on ITO as compared to FTO electrodes.³⁴ The hysteresis at a scan rate of 500 mV/s reduces the V_{oc} and especially the FF when scanning the JV characteristics in forward (short circuit to open circuit) sweep direction. A pronounced hysteresis in perovskite solar cells was attributed to ion migration.⁴⁰⁻⁴⁴ Due to the hysteresis, the V_{oc} and the FF are reduced to 1.05 V and 49.3%, respectively when scanning in forward direction, resulting in an efficiency of the perovskite single junction of 10.4% in forward scan direction.

Interestingly, we found that the influence of the hysteresis in the perovskite sub-cell on the tandem cell characteristics is less pronounced. This finding could potentially be caused by different morphological features on the silicon versus ITO/glass substrate which may affect the ionic movement dynamics. Furthermore, assuming that the hysteresis is originated by ion migration that is field driven, an altered electrical field distribution within the perovskite sub-cell in the monolithic tandem under operation could possibly change the hysteresis behaviour.⁴⁴ The tandem cell exhibits a V_{oc} of 1.785 V which is slightly below the sum of the V_{oc} of both sub-cells in its single junction reference configuration (1.83 V, indicated by the cross in Figure 3). Thus, the measured V_{oc} of the tandem cell is close to the potential value as defined by the respective single junction architectures. Interestingly, the tandem-cell FF of 79.5% is significantly higher than that of both reference single junctions. Using the current calculated from the EQE spectra of the limiting sub-cell (silicon), the efficiency of the tandem in backward scan is 19.9% and the stabilized efficiency using the current measured at MPP over time yields 18.1%. The tandem device also shows a decent stability as almost no difference in the JV characteristics can be found after storing the non-encapsulated tandem devices in inert atmosphere for three months (data not shown). Note that the current measured under the sun simulator calibrated to 100 mW/cm² is slightly smaller as compared to the integrated EQE spectra (see Table 1). This is caused by the shadowing from the soft contact fingers reducing the current that can be generated in the tandem cell when measuring the JV curve, i.e. the current of the limiting sub-cell. In EQE measurements, the monochromated beam size is smaller than the aperture area and thus no shadowing from the contact fingers occurs. Therefore, it is correct to estimate the efficiency using the current calculated from the EQE spectrum of the limiting sub-cell to be the J_{sc} of the tandem.

Just two months after we published our monolithic perovskite/silicon heterojunction tandem cell, Werner and co-workers achieved an even higher efficiency with a comparable tandem architecture.²⁶ They also used a silicon heterojunction together with a perovskite cell that has a low temperature electron selective contact, namely the fullerene derivative PCBM. PCBM is known to reduce the hysteretic behaviour of perovskite solar cells.³¹ Indeed, the tandem cell presented by Werner et al. showed a strongly reduced hysteresis. In addition, they used a textured AR foil to reduce surface reflection and to enhance the photocurrent in parallel. With that, they reached 21.4% from the current voltage scan and a just slightly lower stabilized power output of 21.2%.²⁶

The efficiency evolution of monolithic perovskite/silicon tandem cells from 14 to over 21% during only one year, is remarkable. However, the experimentally realized efficiency is still far below the efficiency expected from fundamental optical simulations.^{45,46} In order to develop an experimental guideline to optically optimize the tandem design further, we have conducted experimentally relevant optical simulations of the monolithic tandem stack utilizing a transfer-matrix approach.⁴⁷ Using a simulated annealing algorithm, we varied the

layer thickness of the perovskite top-cell in the experimentally relevant range (see Figure 4, legend) to find layer-thickness combinations leading to the highest possible photocurrent density under current matching conditions. The layer thicknesses of the silicon heterojunction were kept constant.

Figure 4 displays the absorption (as areas stacked on top of each other, not as a spectrum) of the individual layers in the optically optimized tandem stack that uses the layer thicknesses as indicated in the legend. A rather thin (290 nm) perovskite layer and a thin (thinner than in our experiment) intermediate ITO thickness of 26 nm yields the optimized and matched photocurrent of 17.5 mA/cm² even in the absence of any additional light trapping scheme. This photocurrent can be generated under the assumption that all photons absorbed in the individual sub-cell at the given wavelength generate charges that can be collected at short circuit conditions, which is a good approximation for silicon heterojunctions and perovskite cells.^{20,48}

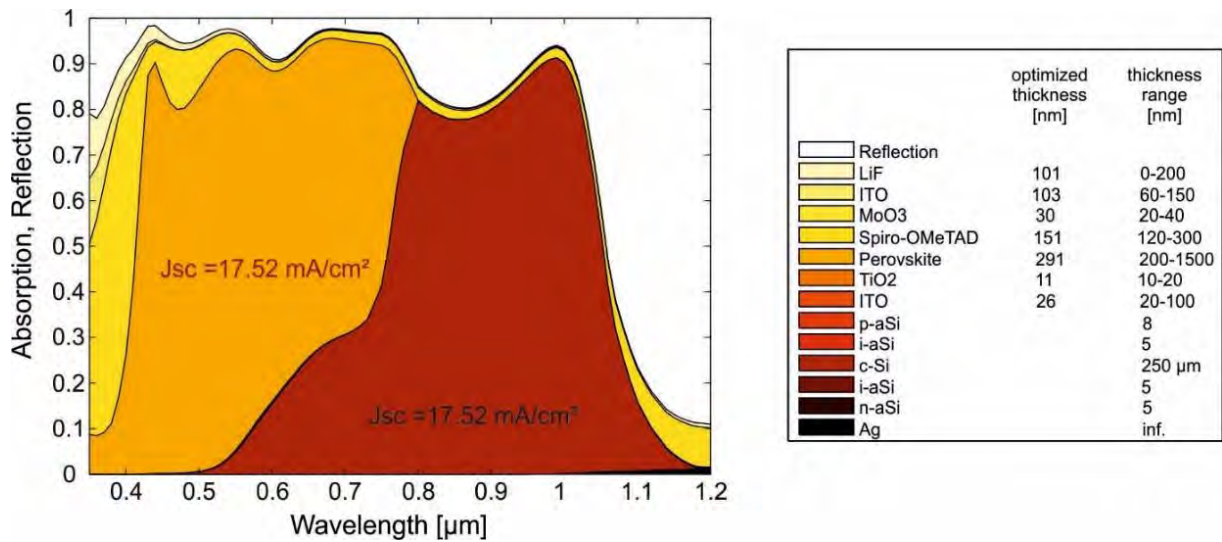


FIG. 4: Breakdown of absorption and reflection vs. wavelength from simulations of monolithic tandem cells under illumination in normal incidence, in which all thicknesses of the perovskite sub-cell and the contact layers have been optimized in experimental relevant thickness ranges (see legend) to get the highest photocurrent density at current matching.

The thin perovskite layer in the optimized tandem stack is necessary as a high portion of light between 600 and 750 nm needs to be transmitted into the silicon bottom cell to achieve current matching. However, this is energetically unfavourable as these photons undergo large thermalization losses. In order to energetically optimize the tandem stack, the optical band-gap of the perovskite needs to be increased.

It was proposed that the optimal band-gap of the perovskite when combined with c-Si in a tandem cell is around 1.74 eV,⁴⁹ which is in agreement with calculations based on the detailed balance limit for tandem cells with different optical band-gaps.²⁸ Recently, McMeekin and co-workers demonstrated that a photostable perovskite based on mixtures of caesium and formamidinium as well as iodide and bromine can be employed to tune the band-gap to 1.74 eV enabling a high V_{oc} of 1.2 eV.⁴⁹

In Figure 5, optical simulations with different perovskite band-gaps are shown. For each band-gap the current-matched J_{sc} is optimized via the thickness optimization routine already used in Figure 4. Interestingly we find that when increasing the band gap from 1.56 eV

towards 1.7 eV in the simulation, the J_{sc} of the tandem cell is not altered. This is caused by the higher optimized thickness that is necessary for the higher band-gap perovskite, as indicated by the orange data points in Figure 5b, left axis. With that, the absorption-onset of the perovskite is sharper and less photons above the perovskite band-gap are transmitted to the silicon for higher band-gaps, leaving the sum of photocurrents of both sub-cells unchanged. This is indicated by the white and grey lines in Figure 5a. Further increasing the band-gap well above 1.7 eV will result in a limitation of the perovskite absorption also for very thick perovskite films with a thickness above 1500 nm, which was set as the maximum experimentally relevant thickness in the simulation (indicated by the orange dashed line in Figure 5(b)). Note that efficient devices with thicknesses up to 3 μm were shown recently utilizing blade coating.⁵⁰ However, further increasing the perovskite thickness from 1.5 to 3 μm for a band gap of 1.78 eV did not significantly enhance the tandem J_{sc} . Thus, the optimum between high J_{sc} and high V_{oc} is found for a band-gap of 1.73 eV (corresponding to an absorption onset of 715 nm) for which 17.48 and 17.47 mA/cm² can be generated in the perovskite and silicon sub-cell, respectively.

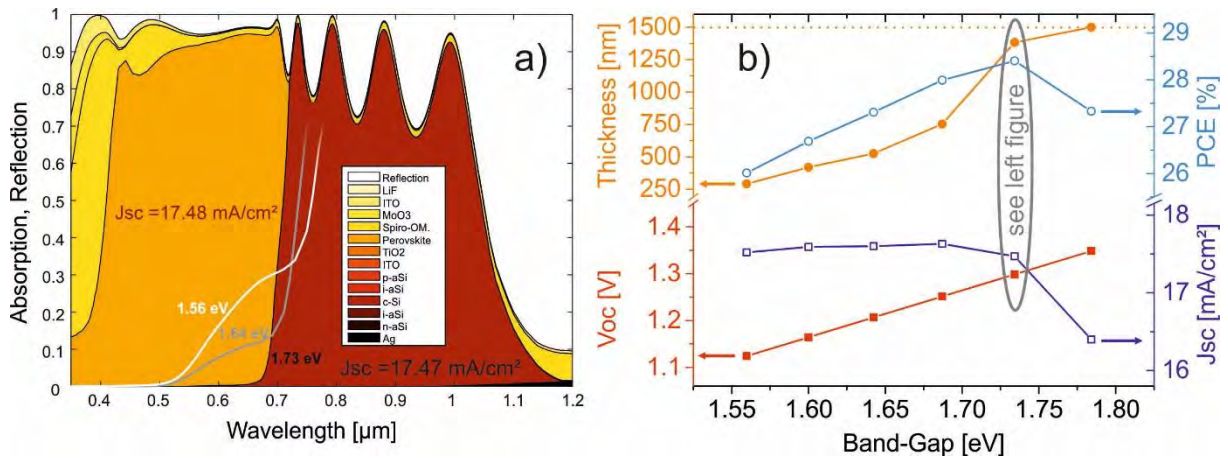


FIG. 5: a) Breakdown of absorption and reflection vs. wavelength from simulations of monolithic tandem cells under illumination in normal incidence, with an optimized perovskite band-gap of 1.73 eV. The thickness of all top-cell layers was optimized within the thickness range presented in Figure 4 to realize the highest photocurrent density. The white and grey lines show the absorption onset of the perovskite sub-cell in tandem stacks with perovskite band-gaps of 1.56 eV and 1.64 eV as indicated. b) Left scale: V_{oc} and optimized film thickness of the perovskite sub-cell. Right scale: J_{sc} and tandem cell efficiency as a function of the used perovskite band-gap. For the efficiency calculation a FF of 81% and a silicon V_{oc} of 709 mV in tandem geometry was assumed.

Based on the experimentally found V_{oc} of 1.13 V for single junction devices, which has been shown for $\text{CH}_3\text{NH}_3\text{PbI}_3$ based devices with EQE onsets around 800 nm,³¹ the V_{oc} of the perovskite sub-cells with higher band gaps is estimated. Here it is assumed that the higher energy of the optical band-gap directly translates into a higher V_{oc} . Note that this has not yet been realized experimentally for a broad optical band-gap range.⁵¹ In the simulation, we include a slight decrease of the perovskite sub-cell V_{oc} in the tandem design of about 6 mV due to the reduced photocurrent generation as compared to the single junction configuration. Further assuming a SHJ V_{oc} of 730 mV in single junction configuration, the V_{oc} in the bottom cell will be reduced by around 21 mV due to the reduced J_{sc} in the tandem. To calculate efficiencies, we assume a FF of 81% which is just slightly above the experimentally achieved record value (data not shown). This results in efficiencies of the tandem device as high as

28.4% for the optimized band gap and thickness combination. Figure 5(a) displays the absorption and reflection for a simulated tandem cell with the optimized band-gap of 1.73 eV and 1383 nm perovskite thickness. For thicker perovskite layers, the absorption edge at the perovskite band gap is very sharp and therefore enables to have current matching at higher band-gaps. In addition, the number of interference fringes increases and with that the overall reflection loss is slightly enhanced for thicker perovskite layers.

CONCLUSION

In conclusion, we reported on the experimental effort aiming at a highly efficient monolithic silicon heterojunction/perovskite tandem solar cell and we summarized different publications showing the tremendous efficiency evolution from 14 to over 21% for this interesting tandem design. In our approach, we combined a planar perovskite sub-cell with SnO₂ as the low temperature electron selective contact formed by ALD and a planar silicon heterojunction. With that we realized a high open circuit voltage between 1.76 and 1.78 V and a fill factor close to 80% that resulted in close to 20% efficiency in reverse scan and 18.1% stabilized efficiency. Importantly, the tandem cell shows an improved efficiency as compared to the reference single junction devices. This result can be further improved as the presented device design is limited by the insufficient absorption in the silicon bottom cell due to losses from reflectance and parasitic absorption. Therefore, we additionally reported on the optical optimization of the tandem cells to present a clear strategy for further device optimization. To further optimize the current matching, we performed optical simulations in which all film thicknesses of the top-cell and its functional layers were optimized to yield the highest photocurrent density in both sub-cells. We have shown that the optimum layer thickness combination is different from the experiment, and it should be possible to produce a high current-matched photocurrent density of around 17.5 mA/cm for this tandem design. We further studied the influence of an increasing perovskite band-gap on the tandem performance in detail and found the optimized band-gap for this device architecture to be around 1.73 eV, using experimentally relevant parameters and the typical parasitic absorption of e.g. spiro-OMeTAD. At this perovskite band-gap, the open circuit voltage should be enhanced to 1.3 V, provided that the energetic increase in band-gap can be directly translated into a higher open circuit voltage. Together with the assumption of a fill factor of 81%, this would result in a planar monolithic tandem cell with an efficiency of 28.4%. The presented results clearly demonstrate the potential of this fascinating type of tandem architecture that has the potential to overcome 30% efficiency when effective light-trapping schemes are implemented.

ACKNOWLEDGEMENTS

The authors would like to thank Thomas Lußky, Erhard Conrad, Kerstin Jacob, Mona Wittig Tobias Hänel, and Karolina Mack from HZB as well as Manuel Hartig from TU Berlin for technical assistance. Marko Jost, Felix Lang and Lukas Kegelmann are acknowledged for lab assistance. Financial support was provided by the European Union Seventh Framework Programme (FP7) through the MESO project (grant no. 604032) and by the Bavarian Ministry for Economics, Media, Energy and Technology through the joint project Hi-ERN.

REFERENCES

- 1) Zhou, H.; Chen, Q.; Li, G.; Luo, S.; Song, T.-b.; Duan, H.-S.; Hong, Z.; You, J.; Liu, Y.; Yang, Y. *Science* **2014**, *345*, 542.
- 2) Jeon, N. J.; Noh, J. H.; Kim, Y. C.; Yang, W. S.; Ryu, S.; Seok, S. I. *Nat Mater* **2014**, *13*, 897.

- 3) http://www.nrel.gov/ncpv/images/efficiency_chart.jpg, accessed 20-04-2016.
- 4) Kojima, A.; Teshima, K.; Shirai, Y.; Miyasaka, T. *Journal of the American Chemical Society* **2009**, *131*, 6050.
- 5) Yang, W. S.; Noh, J. H.; Jeon, N. J.; Kim, Y. C.; Ryu, S.; Seo, J.; Seok, S. I. *Science* **2015**, *348*, 1234.
- 6) Kaltenbrunner, M.; Adam, G.; Glowacki, E. D.; Drack, M.; Schwodiauer, R.; Leonat, L.; Apaydin, D. H.; Groiss, H.; Scharber, M. C.; White, M. S.; Sariciftci, N. S.; Bauer, S. *Nat Mater* **2015**, *14*, 1032.
- 7) Shin, S. S.; Yang, W. S.; Noh, J. H.; Suk, J. H.; Jeon, N. J.; Park, J. H.; Kim, J. S.; Seong, W. M.; Seok, S. I. *Nat Commun* **2015**, *6*, 7410.
- 8) Beal, R. E.; Slotcavage, D. J.; Leijtens, T.; Bowring, A. R.; Belisle, R. A.; Nguyen, W. H.; Burkhard, G. F.; Hoke, E. T.; McGehee, M. D. *The Journal of Physical Chemistry Letters* **2016**, *7*, 746.
- 9) Saliba, M.; Matsui, T.; Seo, J.-Y.; Domanski, K.; Correa-Baena, J.-P.; Mohammad K, N.; Zakeeruddin, S. M.; Tress, W.; Abate, A.; Hagfeldt, A.; Gratzel, M. *Energy & Environmental Science* **2016**, DOI: 10.1039/C5EE03874J.
- 10) Heo, J. H.; Song, D. H.; Im, S. H. *Advanced Materials* **2014**, *26*, 8179.
- 11) Eperon, G. E.; Stranks, S. D.; Menelaou, C.; Johnston, M. B.; Herz, L. M.; Snaith, H. J. *Energy & Environmental Science* **2014**, *7*, 982.
- 12) De Wolf, S.; Holovsky, J.; Moon, S.-J.; Löper, P.; Niesen, B.; Ledinsky, M.; Haug, F.-J.; Yum, J.-H.; Ballif, C. *The Journal of Physical Chemistry Letters* **2014**, *5*, 1035.
- 13) Miyata, A.; Mitiglu, A.; Plochocka, P.; Portugall, O.; Wang, J. T. W.; Stranks, S. D.; Snaith, H. J.; Nicholas, R. J. *Nature Physics* **2015**, *11*, 582.
- 14) Stranks, S. D.; Eperon, G. E.; Grancini, G.; Menelaou, C.; Alcocer, M. J. P.; Leijtens, T.; Herz, L. M.; Petrozza, A.; Snaith, H. J. *Science* **2013**, *342*, 341.
- 15) Xing, G.; Mathews, N.; Sun, S.; Lim, S. S.; Lam, Y. M.; Grätzel, M.; Mhaisalkar, S.; Sum, T. C. *Science* **2013**, *342*, 344.
- 16) Wehrenfennig, C.; Eperon, G. E.; Johnston, M. B.; Snaith, H. J.; Herz, L. M. *Advanced Materials* **2014**, *26*, 1584.
- 17) Xiao, Z.; Dong, Q.; Bi, C.; Shao, Y.; Yuan, Y.; Huang, J. *Advanced Materials* **2014**, *26*, 6503.
- 18) Tress, W.; Marinova, N.; Inganäs, O.; Nazeeruddin, M. K.; Zakeeruddin, S. M.; Graetzel, M. *Advanced Energy Materials* **2015**, *5*, DOI: 10.1002/aenm.201400812.
- 19) Yang, Y.; Yan, Y.; Yang, M.; Choi, S.; Zhu, K.; Luther, J. M.; Beard, M. C. *Nat Commun* **2015**, *6*, 7961.
- 20) Yang, B.; Dyck, O.; Poplawsky, J.; Keum, J.; Poretzky, A.; Das, S.; Ivanov, I.; Rouleau, C.; Duscher, G.; Geohagan, D.; Xiao, K. *Journal of the American Chemical Society* **2015**, *137*, 9210.
- 21) Bi, D.; Tress, W.; Dar, M. I.; Gao, P.; Luo, J.; Renevier, C.; Schenk, K.; Abate, A.; Giordano, F.; Correa Baena, J. P.; Decoppet, J. D.; Zakeeruddin, S. M.; Nazeeruddin, M. K.; Gratzel, M.; Hagfeldt, A. *Sci Adv* **2016**, *2*, e1501170.
- 22) Taguchi, M.; Yano, A.; Tohoda, S.; Matsuyama, K.; Nakamura, Y.; Nishiwaki, T.; Fujita, K.; Maruyama, E. *Photovoltaics, IEEE Journal of* **2014**, *4*, 96.
- 23) Masuko, K.; Shigematsu, M.; Hashiguchi, T.; Fujishima, D.; Kai, M.; Yoshimura, N.; Yamaguchi, T.; Ichihashi, Y.; Mishima, T.; Matsubara, N.; Yamanishi, T.; Takahama, T.; Taguchi, M.; Maruyama, E.; Okamoto, S. *Photovoltaics, IEEE Journal of* **2014**, *4*, 1433.

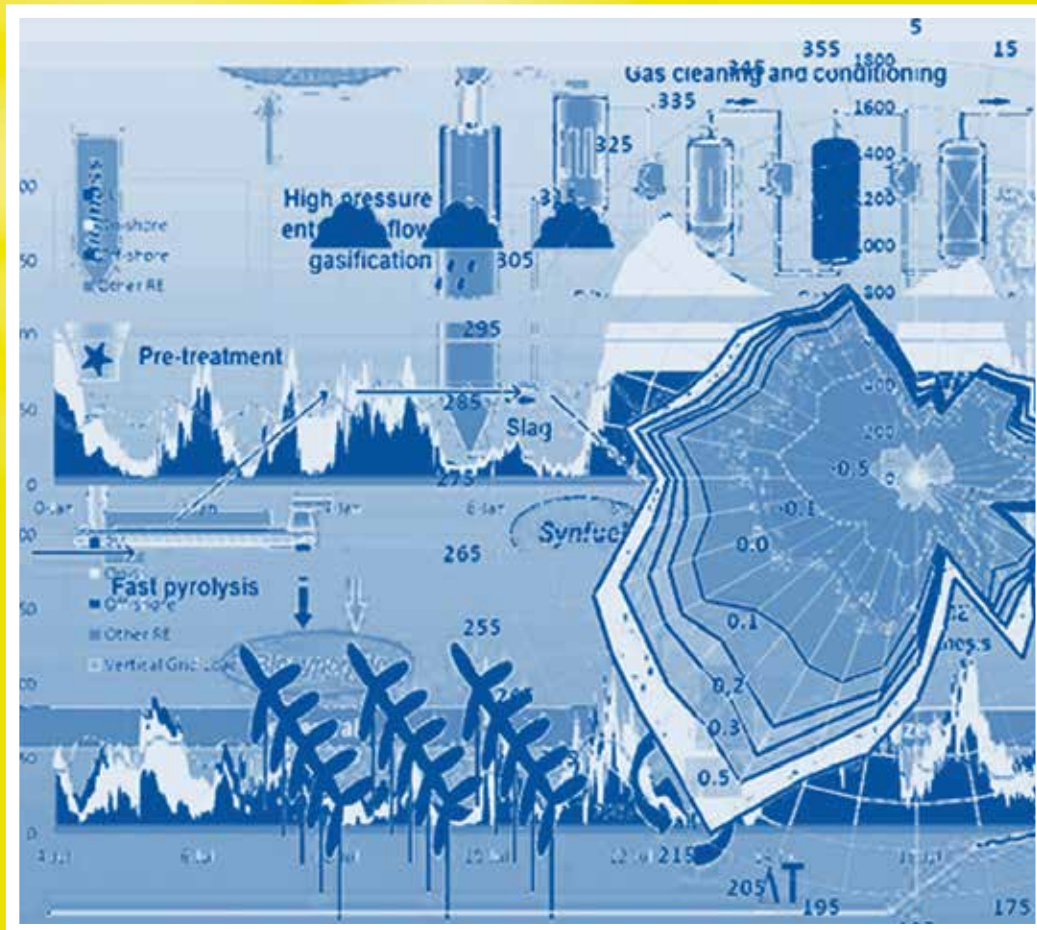
- 24) Glunz, S. W.; Feldmann, F.; Richter, A.; Bivour, M.; Reichel, C.; Steinkemper, H.; Benick, J.; Hermle, M. In *31st European Photovoltaic Solar Energy Conference and Exhibition, Hamburg* 2015.
- 25) Mailoa, J. P.; Bailie, C. D.; Johlin, E. C.; Hoke, E. T.; Akey, A. J.; Nguyen, W. H.; McGehee, M. D.; Buonassisi, T. *Applied Physics Letters* **2015**, *106*, 121105.
- 26) Werner, J.; Weng, C. H.; Walter, A.; Fesquet, L.; Seif, J. P.; De Wolf, S.; Niesen, B.; Ballif, C. *J Phys Chem Lett* **2016**, *7*, 161.
- 27) Albrecht, S.; Saliba, M.; Correa Baena, J. P.; Lang, F.; Kegelmann, L.; Mews, M.; Steier, L.; Abate, A.; Rappich, J.; Korte, L.; Schlattmann, R.; Nazeeruddin, M. K.; Hagfeldt, A.; Grätzel, M.; Rech, B. *Energy Environ. Sci.* **2016**, *9*, 81.
- 28) Vos, A. D. *Journal of Physics D: Applied Physics* **1980**, *13*, 839.
- 29) Shockley, W.; Queisser, H. J. *Journal of Applied Physics* **1961**, *32*, 510.
- 30) Bailie, C. D.; Christoforo, M. G.; Mailoa, J. P.; Bowring, A. R.; Unger, E. L.; Nguyen, W. H.; Burschka, J.; Pellet, N.; Lee, J. Z.; Gratzel, M.; Noufi, R.; Buonassisi, T.; Salleo, A.; McGehee, M. D. *Energy & Environmental Science* **2015**, *8*, 956.
- 31) Tao, C.; Neutzner, S.; Colella, L.; Marras, S.; Srimath Kandada, A. R.; Gandini, M.; Bastiani, M. D.; Pace, G.; Manna, L.; Caironi, M.; Bertarelli, C.; Petrozza, A. *Energy & Environmental Science* **2015**, *8*, 2365.
- 32) Yuan, Z. C.; Wu, Z. W.; Bai, S.; Xia, Z. H.; Xu, W. D.; Song, T.; Wu, H. H.; Xu, L. H.; Si, J. J.; Jin, Y. Z.; Sun, B. Q. *Advanced Energy Materials* **2015**, *5*, DOI: 10.1002/aenm.201500038.
- 33) Ke, W.; Xiao, C.; Wang, C.; Saparov, B.; Duan, H.-S.; Zhao, D.; Xiao, Z.; Schulz, P.; Harvey, S. P.; Liao, W.; Meng, W.; Yu, Y.; Cimaroli, A. J.; Jiang, C.-S.; Zhu, K.; Al-Jassim, M.; Fang, G.; Mitzi, D. B.; Yan, Y. *Advanced Materials* **2016**, DOI: 10.1002/adma.201600594.
- 34) Correa Baena, J. P.; Steier, L.; Tress, W.; Saliba, M.; Neutzner, S.; Matsui, T.; Giordano, F.; Jacobsson, T. J.; Srimath Kandada, A. R.; Zakeeruddin, S. M.; Petrozza, A.; Abate, A.; Nazeeruddin, M. K.; Grätzel, M.; Hagfeldt, A. *Energy Environ. Sci.* **2015**, *8*, 2928.
- 35) Snaith, H. J. *The Journal of Physical Chemistry Letters* **2013**, *4*, 3623.
- 36) Burschka, J.; Kessler, F.; Nazeeruddin, M. K.; Grätzel, M. *Chemistry of Materials* **2013**, *25*, 2986.
- 37) Nguyen, W. H.; Bailie, C. D.; Unger, E. L.; McGehee, M. D. *Journal of the American Chemical Society* **2014**, *136*, 10996.
- 38) Abate, A.; Leijtens, T.; Pathak, S.; Teuscher, J.; Avolio, R.; Errico, M. E.; Kirkpatrick, J.; Ball, J. M.; Docampo, P.; McPherson, I.; Snaith, H. J. *Physical Chemistry Chemical Physics* **2013**, *15*, 2572.
- 39) Kegel, J.; Angermann, H.; Stürzebecher, U.; Conrad, E.; Mews, M.; Korte, L.; Stegemann, B. *Applied Surface Science* **2014**, *301*, 56.
- 40) Tress, W.; Marinova, N.; Moehl, T.; Zakeeruddin, S. M.; Nazeeruddin, M. K.; Gratzel, M. *Energy & Environmental Science* **2015**, *8*, 995.
- 41) Azpiroz, J. M.; Mosconi, E.; Bisquert, J.; De Angelis, F. *Energy & Environmental Science* **2015**, *8*, 2118.
- 42) Eames, C.; Frost, J. M.; Barnes, P. R.; O'Regan, B. C.; Walsh, A.; Islam, M. S. *Nat Commun* **2015**, *6*, 7497.
- 43) Unger, E. L.; Hoke, E. T.; Bailie, C. D.; Nguyen, W. H.; Bowring, A. R.; Heumuller, T.; Christoforo, M. G.; McGehee, M. D. *Energy & Environmental Science* **2014**, *7*, 3690.

- 44) Xiao, Z.; Yuan, Y.; Shao, Y.; Wang, Q.; Dong, Q.; Bi, C.; Sharma, P.; Gruverman, A.; Huang, J. *Nat Mater* **2015**, *14*, 193.
- 45) Filipič, M.; Löper, P.; Niesen, B.; De Wolf, S.; Krč, J.; Ballif, C.; Topič, M. *Optics Express* **2015**, *23*, A263.
- 46) Loper, P.; Moon, S.-J.; Martin de Nicolas, S.; Niesen, B.; Ledinsky, M.; Nicolay, S.; Bailat, J.; Yum, J.-H.; De Wolf, S.; Ballif, C. *Physical Chemistry Chemical Physics* **2015**, *17*, 1619.
- 47) Albrecht, S.; Saliba, M.; Correa-Baena, J.-P.; Jäger, K.; Korte, L.; Hagfeldt, A.; Grätzel, M.; Rech, B. *Journal of Optics* **2016**, *18*, 064012.
- 48) Holman, Z. C.; Descoeurdes, A.; De Wolf, S.; Ballif, C. *Photovoltaics, IEEE Journal of* **2013**, *3*, 1243.
- 49) McMeekin, D. P.; Sadoughi, G.; Rehman, W.; Eperon, G. E.; Saliba, M.; Hörantner, M. T.; Haghighirad, A.; Sakai, N.; Korte, L.; Rech, B.; Johnston, M. B.; Herz, L. M.; Snaith, H. J. *Science* **2016**, *351*, 151.
- 50) Deng, Y.; Peng, E.; Shao, Y.; Xiao, Z.; Dong, Q.; Huang, J. *Energy & Environmental Science* **2015**, *8*, 1544.
- 51) Jesper Jacobsson, T.; Correa-Baena, J.-P.; Pazoki, M.; Saliba, M.; Schenk, K.; Grätzel, M.; Hagfeldt, A. *Energy & Environmental Science* **2016**, *9*, 1706.

Dr. Steve Albrecht¹, Dr. Michael Saliba², Dr. Juan-Pablo Correa-Baena³, Dr. Klaus Jäger⁴, Dr. Lars Korte¹, Prof. Dr. Anders Hagfeldt³, Prof. Dr. Michael Grätzel², and Prof. Dr. Bernd Rech¹

¹ Institute for Silicon Photovoltaics and ⁴Young Investigator Group Nano-SIPPE: Nanostructured Silicon for Photonic and Photovoltaic Implementations, Helmholtz-Zentrum Berlin für Materialien und Energie GmbH, Institut für Silizium-Photovoltaik, Kekuléstraße 5, 12489 Berlin, Germany.

² Laboratory of Photonics and ³Laboratory of Photomolecular Science, Swiss Federal Institute of Technology (EPFL), Station 6, Lausanne CH-1015, Switzerland.



Energie

Forschung und Perspektiven

Vorträge auf der DPG-Frühjahrstagung
Regensburg 2016

Herausgegeben von Hardo Bruhns

Energie

Forschung und Perspektiven

Vorträge auf der DPG-Frühjahrstagung in Regensburg 2016

Arbeitskreis Energie in der Deutschen Physikalischen Gesellschaft

Herausgegeben von Hardo Bruhns

Bad Honnef, August 2016

Frühjahrstagung des Arbeitskreises Energie in der Deutschen Physikalischen Gesellschaft

Regensburg, 6. bis 9. März 2016

Haupt- und Fachvorträge

Inhaltsverzeichnis / Table of Contents

Introduction	7
Fachsitzungen / Sessions	8
Abstracts	9
Globale Klimavariabilität im Industriezeitalter – Phänomene und Ursachen - vorgetragen von Ch. Schönwiese	23
The 2°C climate policy goal: Chances & Challenges - presented by H. Held	35
The reactor accident of Fukushima Dai-ichi and its radiological consequences for the Japanese population - presented by R. Michel	53
Monolithic Perovskite/Silicon Tandem Solar Cells - presented by St. Albrecht	69
Processes for Advanced Fuel Production from Biomass - presented by J. Sauer	83
Methodische Aspekte der Systemanalyse zur Energiewende - vorgetragen von M. Robinius	95

Wasserstoff als Energieträger: Eine Systemanalyse - vorgetragen von S. Schiebahn	103
Offshore Wind Energy - Chances, Challenges, and Impact from a Meteorological Point of View - presented by S. Emeis	113
Wärmepumpe oder KWK – was passt zur Wärmewende? - vorgetragen von G. Luther	123
Impressum	140

Der vorliegende Band versammelt schriftliche Ausarbeitungen von Vorträgen auf der Tagung des Arbeitskreises Energie in der Deutschen Physikalischen Gesellschaft des Jahres 2016 in den Räumen der Universität Regensburg. Leider ist es nicht gelungen, von allen Vortragenden Manuskripte zu erhalten. Die Präsentationsfolien der meisten Hauptvorträge können auf der Webseite des Arbeitskreises über:

<http://www.dpg-physik.de/dpg/organisation/fachlich/ake.html>

(von dort gelangt man zum Archiv des AKE) eingesehen werden. Allen, die zu diesem Sammelband beigetragen haben, sei an dieser Stelle sehr herzlich gedankt.

Düsseldorf, im August 2016

Hardo Bruhns